Wan, X., Xiong, C., Wang, H., Zhang, K., Yin, F. (2020): Spatial characteristics on the occurrence of the nighttime midlatitude medium-scale traveling ionospheric disturbance at topside ionosphere revealed by the Swarm satellite. - Journal of Geophysical Research: Space Physics, 125, 8, e2019JA027739.

https://doi.org/10.1029/2019JA027739

JGR Space Physics

RESEARCH ARTICLE
10.1029/2019JA027739

Spatial Characteristics on the Occurrence of the Nighttime Midlatitude Medium-Scale Traveling Ionospheric Disturbance at Topside Ionosphere Revealed by the Swarm Satellite

Xin Wan[1,3], Chao Xiong[2], Hui Wang[1], Kedeng Zhang[1], and Fan Yin[1]

[1]College of Electronic Information, Wuhan University, Wuhan, China, [2]GFZ German Research Centre for Geosciences, Potsdam, Germany, [3]Planetary Environmental and Astrobiological Research Laboratory (PEARL), School of Atmospheric Sciences, Sun Yat-sen University, Zhuhai, China

Key Points:
- The interhemispheric asymmetry of MSTID shows clear variations on the seasons, local time, longitudes, and solar activity levels
- The horizontal neutral wind and the ionospheric *E-F* region coupling modulate the occurrence of MSTID via Perkins instability
- The band-like enhancement of the plasma benefits the occurrence of MSTID with considerable fluctuation amplitude

Correspondence to:
X. Wan and H. Wang,
iml_wobscene@whu.edu.cn;
h.wang@whu.edu.cn

Citation:
Wan, X., Xiong, C., Wang, H., Zhang, K., & Yin, F. (2020). Spatial characteristics on the occurrence of the nighttime midlatitude medium-scale traveling ionospheric disturbance at topside ionosphere revealed by the Swarm satellite. *Journal of Geophysical Research: Space Physics*, *125*, e2019JA027739. https://doi.org/10.1029/2019JA027739

Received 18 DEC 2019
Accepted 9 JUN 2020
Accepted article online 1 JUL 2020

Abstract Using 6 years collecting of electron density (*Ne*) data from the Swarm A satellite, this study portrays comprehensive maps of the occurrence of medium-scale traveling ionospheric disturbance (MSTID) at middle latitudes, which is characterized by the in situ absolute *Ne* fluctuations above a certain threshold. Two interesting spatial preferences on the occurrence of MSTID as well as their dependence on local time and solar cycle are captured, that is, (1) regional preference near Weddell Sea Anomaly (WSA) to its west during December solstice, MSTID in this region appears even at very low latitudes (at least to 10°N in magnetic latitude) and (2) preference at middle latitudes with a wide zonal extension, which is similar to the recently disclosed nighttime midlatitude plasma band-like enhancement (NMPBE) of the background plasma density (Zhong et al., 2019, https://doi.org/10.1029/2018JA026059). The first preference of MSTID occurring near WSA region can be understood as the effects of horizontal neutral wind contribution to the Perkins instability, with the principal requirement of sporadic *E* occurrence via ionospheric *E-F* region coupling. The fundamental mechanism of the second preference of MSTID occurring includes the interhemispheric coupling that the MSTID can also develop in the winter hemisphere where the local growth rate of Perkins instability is low. Besides, the presence of NMPBE during low solar activity years sets up a favorable environment for the appearance of MSTID with considerable fluctuation amplitude.

1. Introduction

In the nighttime midlatitudes, the medium-scale traveling ionospheric disturbances (MSTIDs) can be frequently observed in the *F* region and the topside ionosphere. The MSTID has a typical horizontal wavelength of 100–500 km with wavefront aligned with northwest (NW)/northeast (NE) to southeast (SE)/southwest (SW) direction in the Northern Hemisphere (NH)/Southern Hemisphere (SH), propagating southwestward/northwestward, in general (e.g., Kotake et al., 2007; Otsuka et al., 2004; Shiokawa, Ihara, et al., 2003; Shiokawa, Otsuka, et al., 2003). The MSTID occurs mostly near two solstices with stronger preference during June solstice at East Asia longitudes (Shiokawa, Ihara, et al., 2003). Global observations showed that the occurrence of MSTID in the summer hemisphere is on average higher than that in the winter hemisphere in terms of the absolute density fluctuations (Park et al., 2010; Watson & Pedatella, 2018). In addition, long-term analysis reveals that the MSTID activity is anticorrelated with the solar cycle (Kotake et al., 2006; Martinis et al., 2010). One interesting feature of MSTID is its conjugate appearance in both the SH and the NH (Otsuka et al., 2004; Shiokawa et al., 2005), which emphasizes the importance of interhemispheric coupling of the ionosphere.

Note that in many aspects, climatology (i.e., seasonal, longitudinal, hemispheric, and solar cycle dependence) or the morphology (i.e., wavefront direction) of MSTID occurrence is very similar to that of sporadic *E* (*Es*) layer (e.g., Arras et al., 2008; Tsai et al., 2018; Zhou et al., 2016), midlatitude electric field fluctuation (MEF), or the midlatitude magnetic field fluctuation (MMF), suggesting tight links between those phenomena (Burke et al., 2016; Park et al., 2009, 2015; Saito et al., 1995, 1998).

It is widely accepted that the generation of MSTID is primarily based on the Perkins instability (Perkins, 1973), supplemented by the coupling processes which can be generalized as the mapping of the

polarization electric field ($\boldsymbol{E}_p$). The latter processes include two categories: (1) *E-F* region coupling via the mapping of the *E* region polarization electric field ($\boldsymbol{E}_P^E$) generated by the *Es* layer (Cosgrove, 2007; Cosgrove & Tsunoda, 2004; Kelley et al., 2003; Tsunoda & Cosgrove, 2001; Yokoyama et al., 2009) and (2) interhemispheric coupling via the mapping of *F* region polarization electric field ($\boldsymbol{E}_P^F$) generated by the MSTID in the source hemisphere (Martinis et al., 2010; Otsuka et al., 2004; Shiokawa et al., 2005). For the detailed coupling process and the associated MEF/MMF signatures, readers are referred to two reviews, Makela and Otsuka (2012) and Yokoyama and Stolle (2017).

However, inadequate global observation and some unresolved problems of MSTID still exist. Most of the works on the conjugacy of MSTID are confined in Japan-Australia longitudes with case studies (Otsuka et al., 2004; Shiokawa et al., 2005). The global observation of the conjugacy of MSTID is rarely reported, although an attempt has been made recently by using satellite observations (e.g., Kil & Paxton, 2017). More importantly, under the absolute fluctuation-based detection criteria, whether/how/why this conjugacy varies in a statistical sense concerning solar activity, seasons, and local time is unknown. Besides, although the MEF and MMF are believed to be highly correlated to the MSTID (Park et al., 2009) climatologically, the intriguing thing is that the signatures of MEF/MMF are not always accompanied with in situ plasma density fluctuations (e.g., Park et al., 2009; Saito et al., 1995).

By exploiting the 6-year Swarm in situ plasma measurements, we present some new properties of midlatitude MSTID in the topside ionosphere, which is characterized by the local electron density fluctuations (Kil & Paxton, 2017; Park et al., 2010; Watson & Pedatella, 2018).

2. Data Set and Processing Method

Swarm is a constellation mission of the European Space Agency (ESA), with three satellites: Alpha (A), Bravo (B), and Charlie (C). They were launched into near-polar orbits on 22 November 2013. Two Langmuir probes onboard each of the satellites provide the electron density along satellite track. In this study, we used the 2-Hz Level 1b data set of electron density (*Ne*) from January 2014 to March 2020 by Swarm A, which flies at an altitude of about 460 km.

Previous studies (e.g., Kil & Paxton, 2017; Park et al., 2010) have validated the assumption that the midlatitude plasma density irregularity/fluctuation should be the consequence of MSTID. Therefore, the *Ne* fluctuations measured by Swarm satellite at middle latitudes are considered to be related to the MSTID in this study. To reduce the geomagnetic disturbance influences on our statistics, we have excluded the Swarm observations when $Kp > 3$.

An algorithm, which is originally designed for the equatorial plasma depletions (EPDs) detection (Wan et al., 2018), is adopted with modifications in this study for detecting the plasma irregularities in middle latitudes. Due to the lower background *Ne* at midlatitudes compared to that at low latitudes, the detection threshold of absolute *Ne* fluctuation is lowered to be 0.08×10^{11} m^{-3}.

However, Swarm electron density data sometimes show artificial anomalies, which are not related to the ionospheric irregularities but are likely connected to the orientation of spacecraft with respect to the Sun. Figure 1 shows two examples of this kind of anomalies, with and without MSTID detected, respectively. In Figure 1a, two kinds of artificial fluctuations can be identified, denoted by the red and green arrows. Based on our experiments, several characteristics of these two kinds of artificial fluctuations can be identified. The first kind of fluctuation (denoted by red arrows) appears at middle latitudes in a group that consists of three to four individual spikes with latitudinal separation of ~3°; these errors occur frequently during 2000–2200 LT. The second kind of fluctuations (denoted by green arrows) appears periodically (latitudinal separation of ~8.5°) with wide latitudinal coverage but has no local time preference. Such kind of artificial fluctuations will affect the detection of MSTID. Therefore, they have to be removed before the statistical analysis is conducted.

To find those artificial fluctuations, a wavelet transformation for locating the high-frequency signals is adopted. Briefly, if the signals appear narrow with certain latitudinal separation (3° for the first and 8.5° for the second kind of artificial fluctuations), they are recognized as artificial fluctuations. Those fluctuations are calibrated by cubic polynomial interpolation. Figure 1b shows the same profile that the artificial signals are removed.

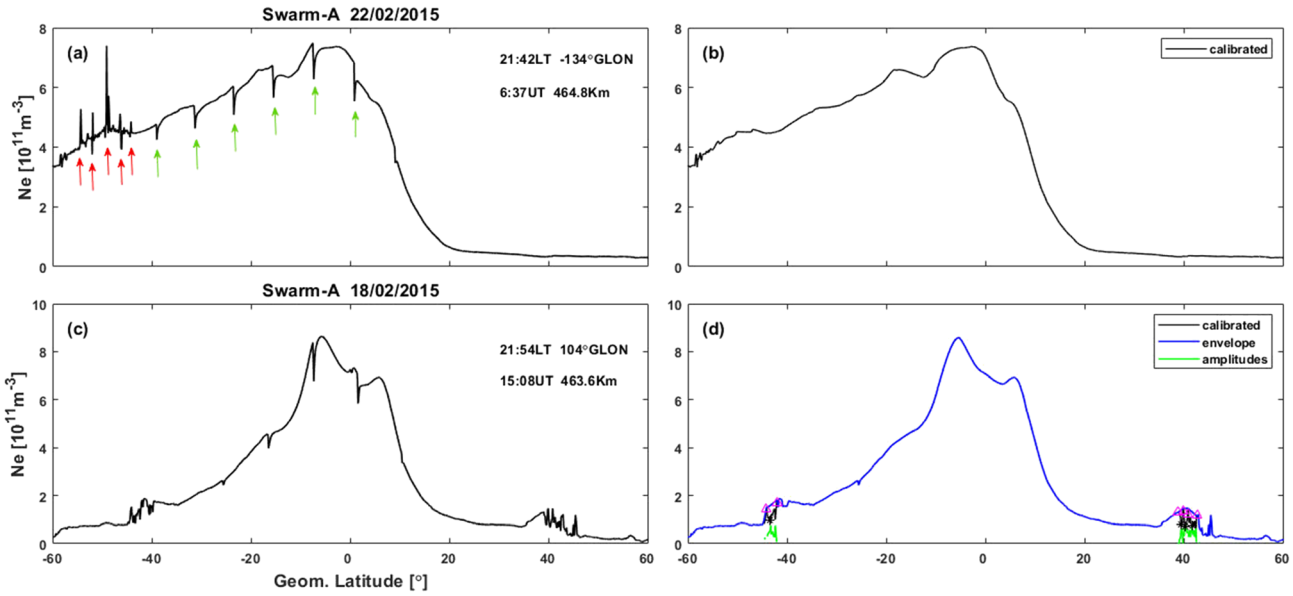

Figure 1. Black lines are the measured *Ne* profile (a, c) without/with MSTID detected (a, b/c, d) and the calibrated *Ne* (b, d). The blue line and green line in (d) are the envelope of *Ne* profile and the fluctuation amplitude of MSTID (the difference between the envelope and calibrated profile), respectively. The red triangles and black asterisks in (c) mark the wave peaks and valleys of the irregularities, respectively. Red and green arrows in (a) denote two kinds of artificial fluctuations.

Figure 1c shows another profile that MSTID and the second kind of artificial fluctuations are both witnessed. We see clearly that the MSTIDs are correctly identified after artificial fluctuation has been removed (Figure 1d). The amplitudes of the MSTID are recorded as green curves. Note that the MSTID is accompanied by background bulges in a width of 10° centered in 40°S/N, which should be the nighttime midlatitude plasma band-like enhancement (NMPBE) as recently reported by Zhong et al. (2019) and Xiong et al. (2019).

The possible relationship between the MSTID and NMPBE will be discussed later, as we had also collected the orbital information when the NMPBE is exhibited in the *Ne* profile. In consideration that the NMPBE is easily masked by the high *Ne* in the summer hemisphere (shown in the next section), the detection of NMPBE focuses on the *Ne* profile in the winter hemisphere. Briefly, the *Ne* profile is first smoothed so that small structures are removed; if the regional peak was found in the latitudinal bin of 33°°S/N to 47°S/N in the winter hemisphere with considerable *Ne* with regard to the ambient, the presence of the NMPBE is confirmed.

Also, to estimate the neutral wind contribution to the Perkins instability, the horizontal wind simulated by the Thermosphere Ionosphere Electrodynamics General Circulation Model (TIEGCM) is adopted. The TIEGCM is a first principle and physics-based model driven by a high-latitude electric field (Heelis et al., 1982), solar extreme ultraviolet and ultraviolet spectral fluxes parameterized by the F10.7 index (Richards et al., 1994).

3. Results

3.1. MSTID During December Solstice

Figure 2 presents the global distribution of the occurrence of ionospheric irregularities at both low and middle latitudes during December solstice (including November, December, January, and February). Data set has been further divided into local time sectors of 1800–2200 LT (postsunset), 2200–0200 LT (midnight), and 0200–0600LT (predawn) separately for different years: 2014–2015, 2016–2017, and 2018 to March 2020 (2018–2020) for representing different solar activities. The averaged F10.7 index for the three 2-year periods is 133 (moderate solar flux), 83 (low solar flux), and 70 sfu (very low solar flux). A prominent feature of the irregularities is the prevalence of the irregularities at equatorial and low latitudes, which agrees well with previous studies on the EPDs (e.g., Stolle et al., 2006; Su et al., 2006; Wan et al., 2018). As the EPD is not the main topic of this study, in the rest of this paper, we will focus mainly on the MSTID in the midlatitudes.

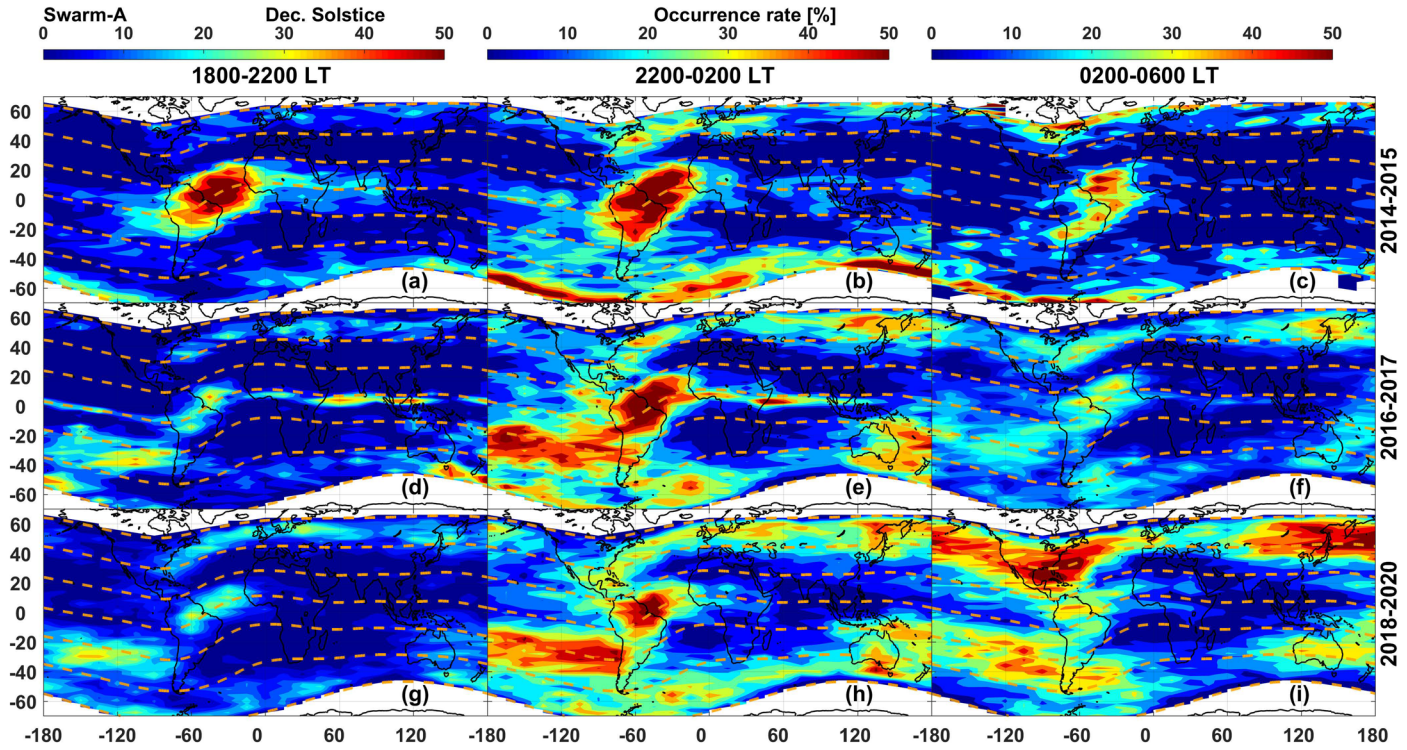

Figure 2. (a–i) Geographical distribution of the occurrence rate of MSTID. The dashed lines mark the magnetic latitude from −60°N to 60°N in the step of 20°.

Note that the high occurrence rate near −60°N in magnetic latitude during 2014–2015 is not caused by the MSTID but the plasma irregularities related to subauroral activities; a similar phenomenon can be witnessed during June solstice as shown in the next subsection.

The MSTID occurrence has a longitudinal preference from southeast Pacific to South America, which is a persistent phenomenon from low to middle latitudes in the SH during all three local time sectors (i.e., Figures 2e and 2h). Near the west coast of South America, the MSTID can even appear at places very close to the equatorial region. We infer that those equatorial irregularities are MSTID but not EPDs for the reason that EPDs cannot get developed from off-equator since the polarization electric field will be short out by the high-conductivity equatorial ionosphere through the field line. If those irregularities at the southside of the magnetic equator are the EPDs, there should be more at the magnetic equator, which is not exhibited in Figure 2.

Figure 3 gives the same distribution of the background electron density (*Ne*). Coincidently, the contour of background *Ne* exhibits an abnormal enhancement in the same region (Figures 3b, 3c, 3e, and 3f), which has been termed as Weddell Sea Anomaly (WSA). The same longitudinal preference near WSA of MSTID has been previously captured (Park et al., 2010; Wan et al., 2018; Watson & Pedatella, 2018), but the reason has not been answered yet, to our knowledge. Moreover, the occurrence of the MSTID shows an increase from 2014–2015 to 2016–2017 and stays at a high level during 2018–2020, throughout the whole night.

Less popular regions with MSTID occurrence during 2014–2015 lie among the north America, Atlantic, Europe, and East Asia in the NH. With solar activity decreasing, the occurrence in these regions is significantly increased especially for the local time sector of predawn (Figure 2i). From the perspective of local time, we find that the occurrence of MSTID generally peaks around the midnight sector. However, during 2017–2020 which correspond to the very low solar activity, the MSTID occurrence in the NH peaks at the predawn sector.

From a global scale, for the local time sectors of midnight and predawn, the MSTID occurrence tends to show a band-like distribution (narrow meridional strip near 40°N with wide zonal extension in the North America-Europe-Asia sector) first in the NH during 2016–2017 (Figures 2e and 2f). Similar band-like

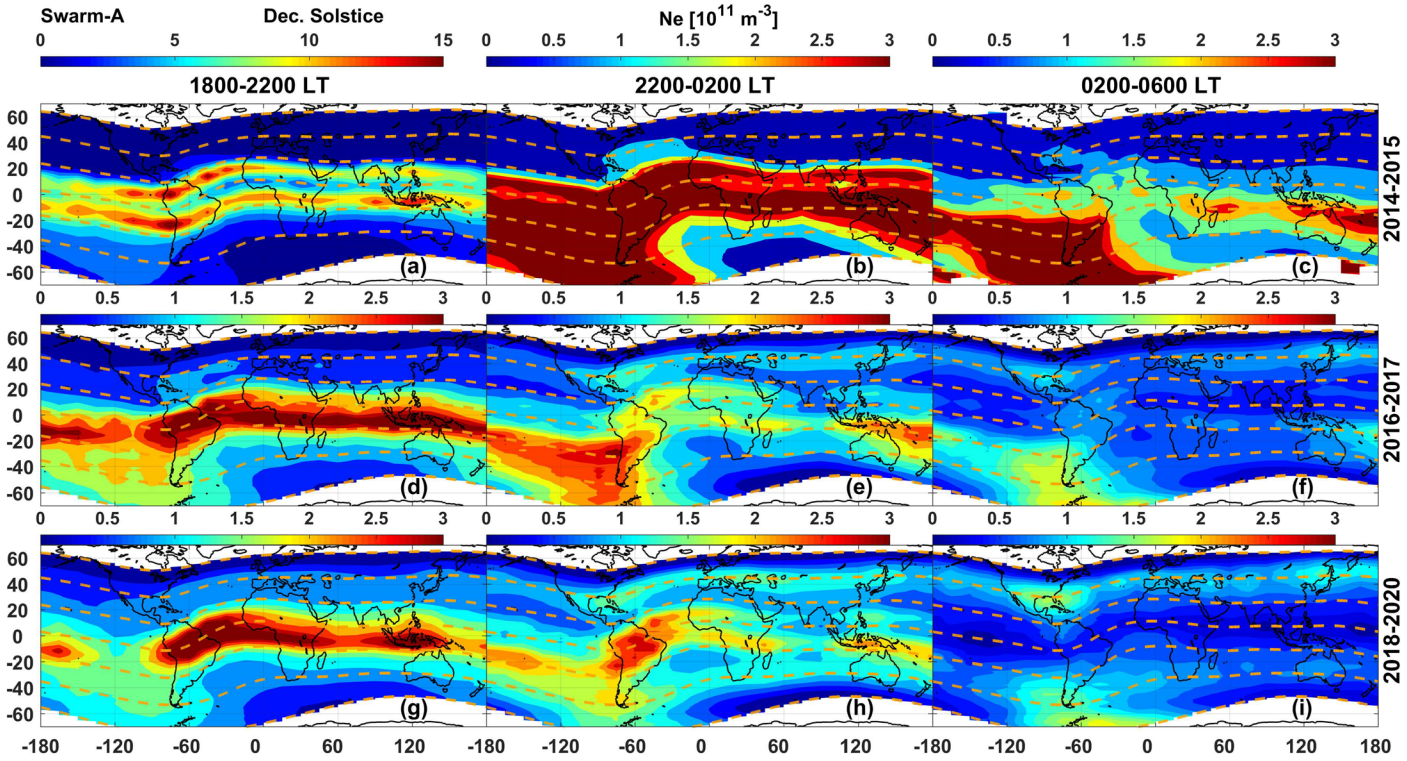

Figure 3. Same as Figure 2 but for the electron density (*Ne*).

distribution is subsequently developed during 2018–2020 (Figures 2h and 2i) for both hemispheres, as the occurrence of MSTID at the American-Atlantic sector in the SH is increased. The MSTID is more frequently observed in the SH than that in the NH at postsunset and midnight. However, for the predawn local time sector, the occurrence of MSTID in the NH exceeds that in the SH.

Coincidently, the NMPBE located in the same region of the higher MSTID occurrence first emerges from 2016–2017 (Figures 3e and 3f) for the NH and subsequently appears in both SH and NH during 2018–2020. A mild increase of *Ne* in the northern midlatitudes at midnight and predawn is identified from 2014–2015 through 2016–2017 to 2018–2020, which is anticorrelated with the solar activity. However, we want to emphasize that the similarity between MSTID occurrence and background *Ne* is not purely caused by our absolute fluctuation-based detection algorithm. Shreds of evidence can be raised; for example, the occurrence of MSTID near WSA is increased from 2014–2015 to 2016–2017 and 2018–2020 while the background *Ne* is decreased in the same region; the peak *Ne* at North America keeps in the same level as shown in Figures 3e, 3h, and 3i; however, quite large variations of corresponding MSTID occurrence can be observed among Figures 2e, 2h, and 2i.

3.2. MSTID During June Solstice

Figure 4 shows the occurrence of ionospheric irregularities during June solstice (May, June, July, and August). Similar to that of December solstice during 2014–2015, the occurrence rate is high near 60°N, which should also be related to auroral activities. Focusing on the MSTID in midlatitudes, during 2014–2015, MSTID prevails in the NH (Figures 4a–4c). Again, MSTID generally shows maximum occurrence at midnight, with a major peak at the Asia-Pacific and a minor peak at America-Atlantic longitudes. As the local time sector moves to predawn, the occurrence of MSTID is decaying. Besides, the MSTID in the SH does not change much as local time moves. The situation changes in which the occurrence of MSTID in the SH is significantly enhanced from postsunset to midnight and keeps at a high level until predawn as solar activity decreases during 2016–2017 and 2018–2020.

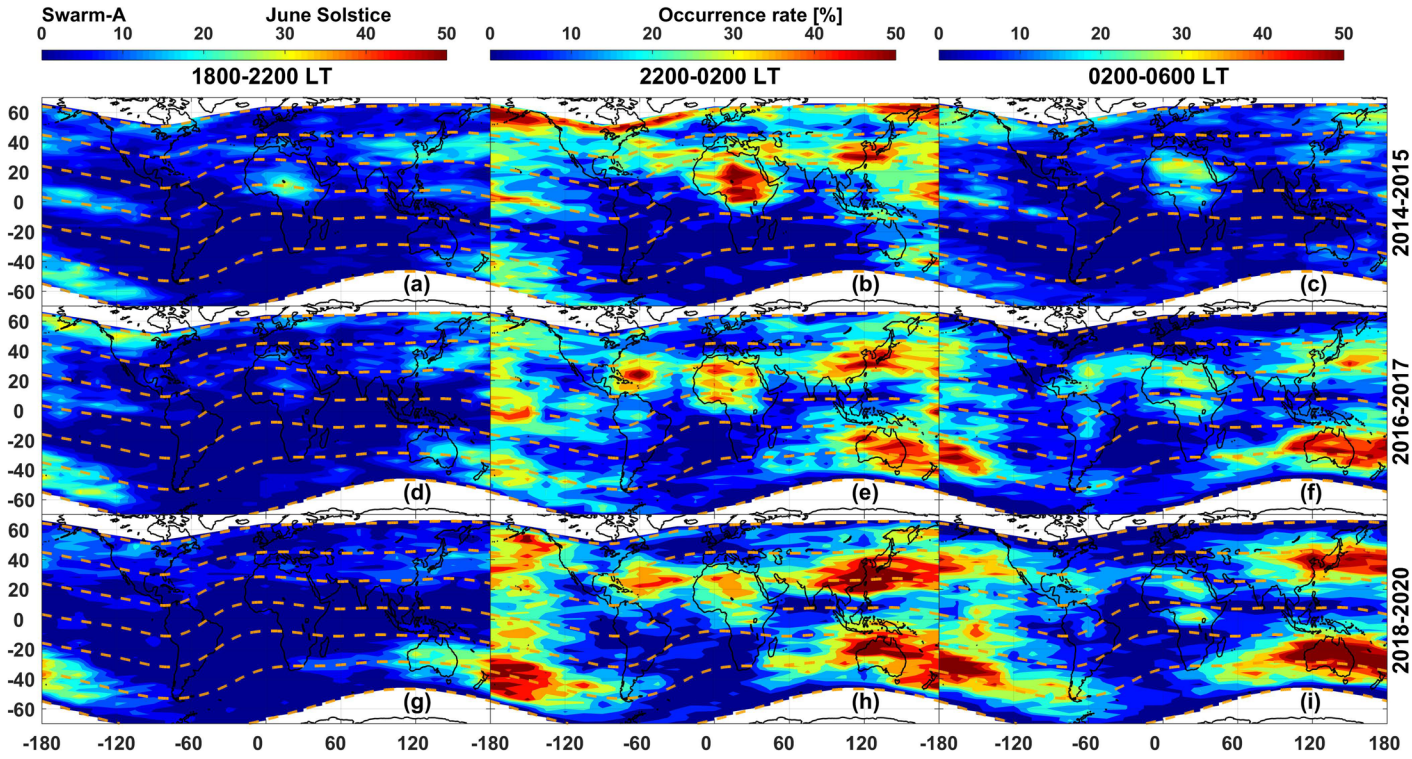

Figure 4. Same as Figure 2 but for the period during June solstice.

The occurrence of MSTID shows different solar cycle variations in different local time sectors. At postsunset (Figures 4a, 4d, and 4g), the occurrence of MSTID in both hemispheres does not change much from 2014–2015 to later years, neither on the longitudinal coverage nor the magnitude. However, the occurrence of MSTID in both hemispheres at midnight and predawn is enhanced as the solar cycle reaches the solar minimum. The enhancement is more significant in the SH. Similar to that during December solstice, the occurrence of MSTID in the NH is stronger than that in the SH during 2014–2015 (Figures 4a–4c). As solar activity decreases and local time moves to predawn, this hemispheric asymmetry changes or even reverses (Figures 4e–4i).

Nevertheless, the band-like distribution of the MSTID occurrence is again witnessed especially during solar minimum, which covers most of the longitudinal sector except in the south Atlantic region where the occurrence of MSTID persistently keeps at a low level. Toward the similar longitudinal band distributions, we inspect the distribution of the background *Ne* as shown in Figure 5. During 2014–2015, the *Ne* enhancement is only visible for the predawn sector in the SH (Figure 5c); for postsunset, the same enhancement at SH is only visible during 2018–2020 near Australia (Figure 5g). Moreover, as solar activity level goes down and at later local time hours, the NMPBEs are found not only in the SH but also in the NH, and they become more and more prominent (Figures 5f, 5h, and 5i). All these results suggest that the NMPBEs appear preferentially at postmidnight during low solar activity years, which is consistent with Zhong et al. (2019). Similar to that in December solstice, the increase of *Ne* at the southern midlatitude from 2014–2015 through 2016–2017 to 2018–2020 is witnessed.

3.3. Summary of the Observational Facts

Generally, the dependences of MSTID occurrence on the season, solar cycle, longitudes, and local time are in good agreement with previous studies (Kotake et al., 2006; Park et al., 2009; Shiokawa et al., 2005; Watson & Pedatella, 2018, and references therein). In supplement to previous findings, some interesting features are revealed in this study. At the postsunset sector, the anticorrelations between the occurrence of MSTID and the solar cycle are not as evidenced as in midnight or predawn. Besides, two interesting features of MSTID occurrence can be captured: (1) regional preference of MSTID occurrence near the WSA and its

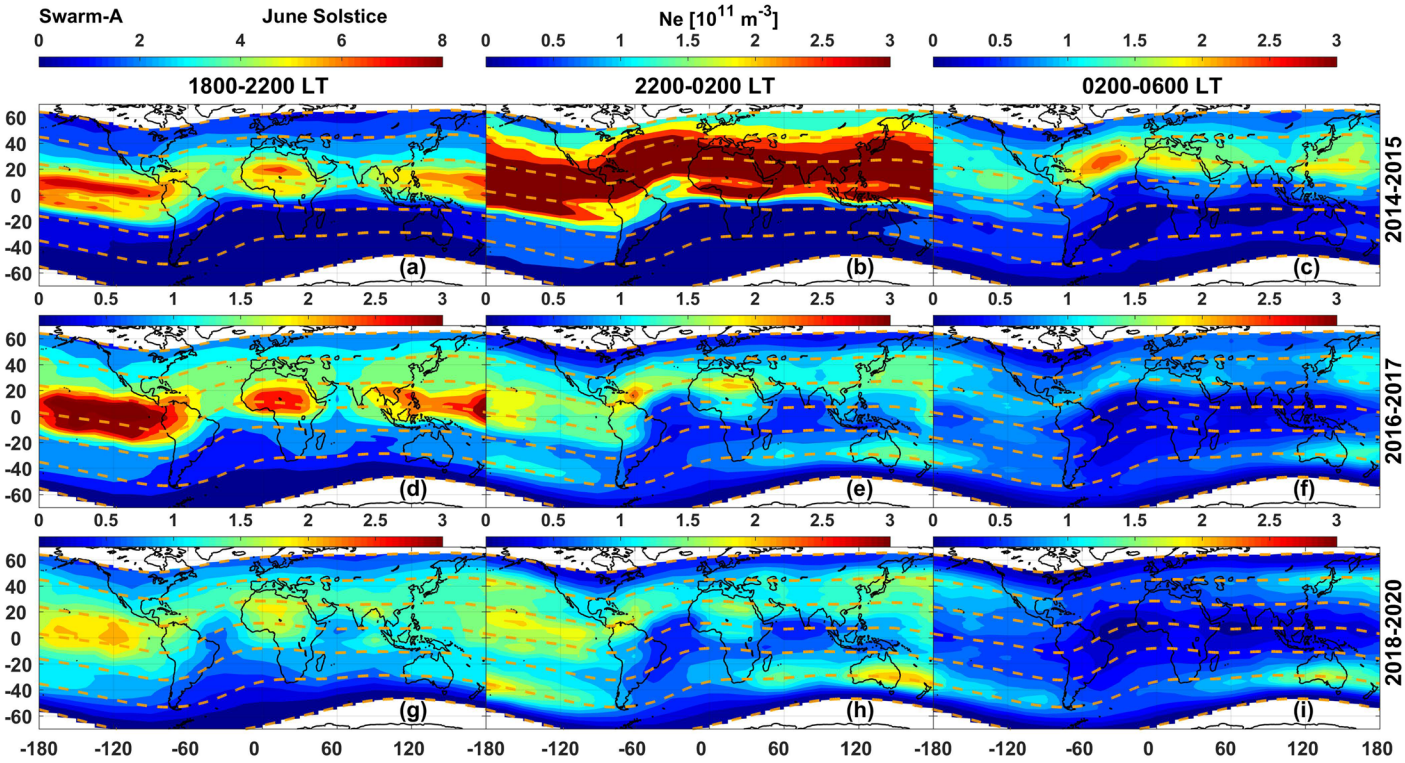

Figure 5. Same as Figure 4 but for the electron density.

westside during December solstice, reaching very low latitudes in these longitudes, and (2) longitudinal band-like distribution of MSTID at middle latitudes for both solstice seasons. In the following, we refer the above two phenomena as "first" and "second" issues.

The evolution of the longitudinal band-like distribution at middle latitudes is rather interesting that in the winter hemisphere it is significantly enhanced as solar activity declines and local time toward postmidnight hours. Together with the existing MSTID in the summer hemisphere, the longitudinal double-band distribution in both hemispheres is formed. In other words, hemispheric asymmetry of MSTID occurrence develops into hemispheric symmetry (or even reverses) from moderate to low solar activity years, from midnight to predawn sector.

Meanwhile, the background *Ne* distribution shows a similar solar cycle/local time evolution with the occurrence of MSTID on the two issues. Besides, the plasma density (i.e., *Ne* in summer hemisphere shown in our plots) is generally positively correlated with the solar flux which dominated the photoionization process for producing plasma. However, the midlatitude *Ne* in winter hemisphere is anticorrelated with the solar flux, under the presence of NMPBE. The downward filling of plasma from plasmasphere might be the cause of this usual enhanced *Ne* during low solar flux years (Xiong et al., 2019; Zhong et al., 2019).

4. Discussion

Based on the fact that the wavefront of MSTID is geomagnetically aligned along the NW-SE (NE-SW) direction in NH (SH) in most circumstances, the southeastward (northeastward) *F* region neutral wind, which results in effective electric field in northeastward (southeastward) direction, is required to induce the Perkins instability (Makela & Otsuka, 2012). Chen et al. (2011) theoretically examined the major role of equatorward wind for the cause of WSA while the downward flux from the plasmasphere provides a secondary source. The overlapping of the high occurrence of MSTID with WSA (first issue) indicates that there might be the same processes to benefit the two phenomena. Besides, Zhong et al. (2019) suggested that

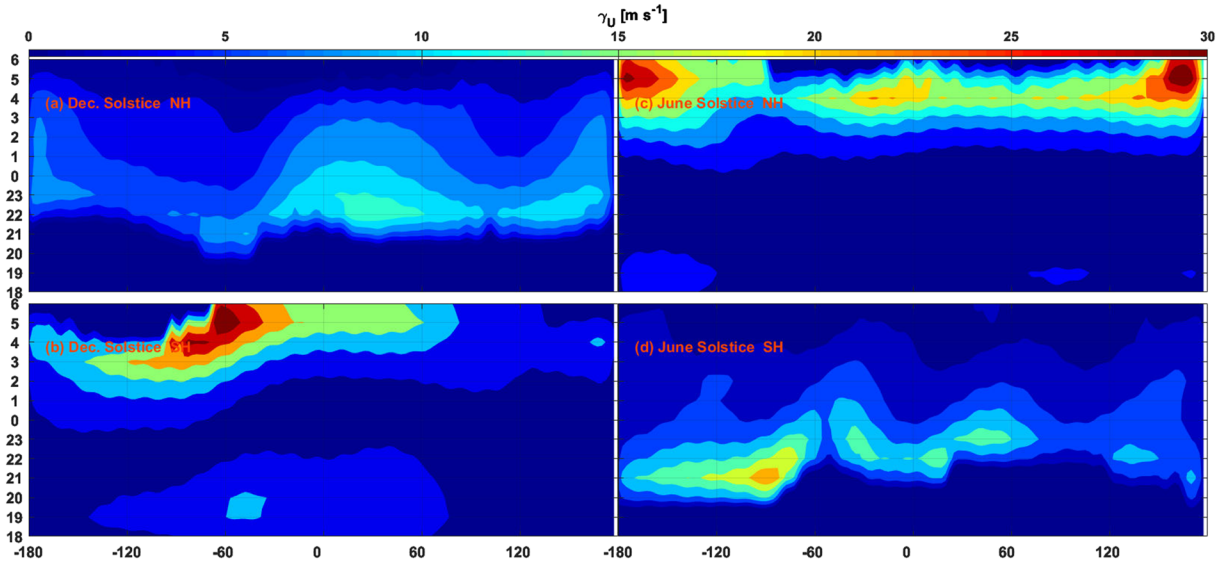

Figure 6. The maximum contribution from *F* region horizontal neutral wind to the Perkins instability as a function of geographic longitudes versus local time at midlatitudes (30°S/N to 50°S/N).

the enhanced equatorial wind will help to push the plasma along the field line up to higher altitude at the middle latitude, accumulate at the topside ionosphere, and form the NMPBE.

Thus, it is reasonable that the neutral wind should bring some beneficial conditions to the aforementioned two issues. According to Garcia et al. (2000), the neutral wind contribution to the Perkins instability in one hemisphere of MSTID can be written as

$$\gamma_U = -\frac{\cos D \sin D}{H_n}\boldsymbol{U}_{eq,\,mag} + \frac{\boldsymbol{k}_y \cos D}{\boldsymbol{k}^2 H_n}\left[\boldsymbol{k}_x \boldsymbol{U}_{e,\,mag} + \sin D \boldsymbol{k}_y \boldsymbol{U}_{eq,\,mag}\right] \tag{1}$$

where D is the dip angle, H_n denotes the atmospheric scale height, $\boldsymbol{k}$ is the wave vector of MSTID, $\boldsymbol{k}_x = \boldsymbol{k}\sin\theta$ and $\boldsymbol{k}_y = \boldsymbol{k}\cos\theta$ are the magnetic meridional and east component of the wavenumber, and θ is the angle between wave vector and magnetic east direction. $\boldsymbol{U}_{e,mag} = \boldsymbol{U}_e\cos\delta + \boldsymbol{U}_s\sin\delta$ denotes the magnetic eastward neutral wind, where $\boldsymbol{U}_e$ and $\boldsymbol{U}_s$ are the eastward zonal and southward meridional wind in geographical coordinate, respectively, and δ is the magnetic declination. $\boldsymbol{U}_{eq,mag} = \pm(\boldsymbol{U}_e\sin\delta - \boldsymbol{U}_s\cos\delta)$ is the horizontal wind component confined within the magnetic meridional plane; positive/negative sign denotes the equatorward wind in the SH/NH. Because the electric field at nighttime is generated by the *F* region dynamo, the direction of the effective electric field would be close to the direction of $\boldsymbol{U}_{mag} \times \boldsymbol{B}$ (Makela & Otsuka, 2012). The maximum γ_U happens when the wave vector lies in the middle angle between the effective electric field (should be with eastward component) with the magnetic east (Garcia et al., 2000; Makela & Otsuka, 2012). The angle of the effective electric field with regard to the magnetic east could be written as $\alpha = arctan\frac{\boldsymbol{U}_{e,\,mag}}{\boldsymbol{U}_{eq,\,mag}}$; thus, $\theta = \frac{\alpha}{2}$, $\boldsymbol{k}_x = \boldsymbol{k}\sin\left(0.5{*}arctan\frac{\boldsymbol{U}_{e,\,mag}}{\boldsymbol{U}_{eq,\,mag}}\right)$, and $\boldsymbol{k}_y = \boldsymbol{k}\cos\left(0.5{*}arctan\frac{\boldsymbol{U}_{e,\,mag}}{\boldsymbol{U}_{eq,\,mag}}\right)$. When we ignore H_n by assuming that it does not change much at midlatitude, the maximum wind contribution to Perkins instability could be written as

$$\begin{aligned}\gamma_{U,\,max} &\propto -\sin D\cos D\boldsymbol{U}_{eq,\,mag} + \cos\theta\cos D\left[\sin\theta\boldsymbol{U}_{e,\,mag} + \sin D\cos\theta\boldsymbol{U}_{eq,\,mag}\right] \\ &\propto -\sin D\cos D\sin^2\theta\boldsymbol{U}_{eq,\,mag} + \cos D\cos\theta\sin\theta\boldsymbol{U}_{e,\,mag}\end{aligned} \tag{2}$$

Figure 6 presents the $\gamma_{U,max}$ at middle latitudes (30–50°) as a function of geographic longitudes and local time. The calculation is based on the TIEGCM-derived quiet-time horizontal neutral wind vector at low

solar flux level (F10.7 = 70 sfu). The lower boundary condition of TIEGCM running is derived from the Sounding of the Atmosphere using Broadband Emission Radiometry (SABER) and TIDI observations, which include both the migrating and the nonmigrating tides. The magnetic inclination and declination are derived from the CHAOS-6 model at an altitude of 250 km.

We had also tested the calculations at the satellite altitude of 460 km during high (F10.7 = 180 sfu) and moderate (F10.7 = 140 sfu) solar activities. The results are almost the same as the presented pattern shown in Figure 6.

Generally, $\gamma_{U,max}$ is strongest at local summer which corresponds well with our and previous observations (e.g., Hernández-Pajares et al., 2012; Park et al., 2010). During June solstice, $\gamma_{U,max}$ has a major peak at east Asia-Pacific, a median peak at Europe, and a minor peak at Atlantic in the NH. During December solstice, the $\gamma_{U,max}$ at SH has two peaks that lie at both sides of the meridian line of −60°W where the magnetic declination changes its polarization and the center of WSA locates. We note that the similarities exist between the $\gamma_{U,max}$ with the occurrence rate of MSTID on their longitudinal variation in the summer hemisphere. The major disagreement of this longitudinal correlation lies near the eastern peak of the $\gamma_{U,max}$ in the SH during December solstice in which the occurrence rate of MSTID is not high. The explanation will be addressed later.

$\gamma_{U,max}$ is larger at the postsunset (postmidnight) for winter (summer) hemisphere during two solstices. This local time/hemispheric variation is different from our observation that the MSTID in the summer hemisphere is strong at midnight, while in the winter hemisphere, it prevails at later local time. Besides, $\gamma_{U,max}$ shows no conjugate signature which can neither explain the MSTID occurrence distribution in the both hemispheres during deep solar minimum. The contradiction indicates that the growth of $\gamma_{U,max}$ is not adequate to answer the local time dependence or the conjugacy of the MSTID occurrence.

One of the major problems with the Perkins instability theory is that the growth rate is very slow (Kelley & Makela, 2001). The problem is solved by taking the coupling between the *E* and *F* regions into account. Cosgrove and Tsunoda (2004) showed that a coupled system including *E*s instability gives a larger growth rate of Perkins instability. The theory is supported by the simulation of Yokoyama et al. (2009), who further concluded that the *E*s plays a major role in seeding *F* region MSTID and the Perkins instability is required to amplify the perturbation.

Since *E*s activity is rare in the winter hemisphere (Arras et al., 2008; Niu et al., 2019; Tsai et al., 2018; Zhou et al., 2016), the considerable contribution from $\gamma_{U,max}$ at postsunset in the winter hemisphere (Figures 5a and 5e) cannot be amplified to trigger irregularities. Thus, MSTID activity is rare at postsunset. The largest growth rate coincidently exists in the summer hemisphere; however, the local time preference is postmidnight while the nighttime *E*s is mainly a premidnight phenomenon (Haldoupis & Schlegel, 1996; Tsai et al., 2018; Wu et al., 2005; Zhou et al., 2016). Note that the zonal wind component derived from TIEGCM turns from weak eastward to strong westward with transition time lying at premidnight (not shown). Compared to the observations (e.g., Jiang et al., 2018; Xiong et al., 2015), the modeling underestimates the eastward wind velocity at premidnight, which may further underestimate $\gamma_{U,max}$. Nevertheless, we see that the occurrence of MSTID is low at postsunset, which may result from the low $\gamma_{U,max}$ even if the occurrence of *E*s is high. $\gamma_{U,max}$ starts to show considerable intensity from midnight and peaks at the predawn sector. Considering that the *E*s prefers premidnight, the latter stage of the *E*s activity meets the early stage of the high $\gamma_{U,max}$, at the midnight sector, which may lead to that the strongest growth rate of *E-F* layer coupled Perkins instability. The local time configuration of *E-F* layer coupled Perkins instability should be accounted for the high occurrence of MSTID at midnight and predawn.

However, we note that the neutral wind is mainly westward (e.g., Xiong et al., 2015) and equatorward at the predawn sector in the summer hemisphere, so as for our TIEGCM modeled neutral wind (not shown). Under this configuration, the wavefront of the MSTID should be aligned in NE-SW and NW-SE direction in the NH and SH, which is perpendicular to the most observed direction of MSTID as mentioned above (e.g., Kotake et al., 2007; Otsuka et al., 2004; Shiokawa, Ihara, et al., 2003; Shiokawa, Otsuka, et al., 2003). Some underlying issues should be explored to solve the discrepancy between the simulation and observation. Since the single satellite observation cannot provide information on the direction of MSTID, further works are needed.

The longitudinal discrepancy between the $\gamma_{U,max}$ with the MSTID occurrence can also be answered by the *E*s. For December solstice in SH, the *E*s prevails at all the longitudes except the south Atlantic sector (Arras et al., 2008; Tsai et al., 2018) which corresponds to the eastside of WSA (eastern peak of $\gamma_{U,max}$). Thus, MSTID only prevails near WSA and its westward edge. We suggest that the combined effects of *F* region wind with the *E*s activity on the Perkins instability determine the seasonal/longitudinal/local time dependence of the MSTID occurrence in the summer hemisphere, which also explains the first issue.

$\gamma_{U,max}$ barely varies with the solar cycle since the background electric field, which is inversely correlated with the ion-neutral collision frequency is not included. We note that the full expression of the Perkins instability is inversely correlated with the ion-neutral collision frequency, so as the neutral density which decreases with decreasing solar activity (Fuller-Rowell, 1998). Thus, the enhanced occurrence rate of MSTID is promised during the solar minimum (Kotake et al., 2006).

Till now, the second issue is still not resolved since both the wind contribution of Perkins instability and the *E*s occurrence rate is stronger in the summer hemisphere regardless of solar activity level. Conjugate existence of the MSTID in both hemispheres has been observed mainly by case studies in Japan and Australia (Otsuka et al., 2004; Shiokawa et al., 2005). The mechanism highlights the interhemispheric mapping of the $\boldsymbol{E}_{\mathrm{p}}$ generated by the MSTID in the source hemisphere (Otsuka et al., 2004; Martinis et al., 2010; Shiokawa et al., 2005). The source hemisphere should be the summer hemisphere as explained above. Simulations on the hemispheric coupling had deduced a quite optimistic mapping efficiency (Saito et al., 1995, 1998). Other supporting evidence is that the MEF and MMF, which are believed to be the signals of MSTID as they show many similarities with MSTID climatologically, exhibit more conjugated distribution (Park et al., 2009, 2015; Saito et al., 1995, 1998). Thus, the higher occurrence of MSTID in the winter hemisphere during low solar flux years should be attributed to the interhemispheric coupling. Besides, the interhemispheric coupling process should affect the Perkins instability which is not considered in the first order when we calculate $\gamma_{U,max}$. That is, if we assume that the instability in the source hemisphere is stronger, the coupling process would destabilize the opposite hemisphere or stabilize the source hemisphere depending on whether the opposite hemisphere is suitable for the growth of the Perkins instability. However, we see that the $\gamma_{U,max}$ has clear local time bias between two hemispheres ($\gamma_{U,max}$ is high at premidnight/postmidnight in winter/summer hemisphere). Besides, as discussed above, the longitudinal dependence of the MSTID's occurrence is well explained by the coupled system of $\gamma_{U,max}$ with *E*s occurrence. Thus, the interhemispheric coupling would have less effects on the longitudinal variation of MSTID but on the conjugated appearance of the MSTID.

However, a remaining question is why MSTID in the winter hemisphere is evidently lower compared to the summer hemisphere during moderate solar flux years (2014–2015). Please note that other global observations based on the absolute criteria detection method also report the summer hemisphere preference of MSTID (Park et al., 2009; Watson & Pedatella, 2018). Kil and Paxton (2017), who adopt the relative fluctuation criteria for the detection of MSTID from Swarm electron density observations during 2014–2017, have found hemispheric symmetry of MSTID occurrence in a statistical sense. In their methods, the irregularities with rather small fluctuation amplitudes (with magnitude smaller than the background *Ne* in orders) could also be detected.

MSTID is created by the upward and downward moving of the ionospheric plasma due to the polarization electric field. As elucidated in Park et al. (2009) under the same instability growth rate, the fluctuation of *Ne* is higher when higher background *Ne* and the lower plasma scale height is exhibited in the summer hemisphere compared to that in the winter hemisphere. Thus, the background condition determines the intensity of the plasma fluctuation caused by the MSTID. As we noted that under the presence of NMPBE during 2016–2017 and 2018–2020, the midlatitude *Ne* in winter hemisphere is increased from 2014–2015 through 2016–2017 to 2018–2020, the plasma fluctuation level should also be increased. Since our detection involves the absolute criteria, for the winter hemisphere, more MSTID events would be detected during lower solar activity years. Thus, a much clearer conjugated signature of MSTID in both hemispheres appears during 2016–2017 and 2018–2020 compared to that during 2014–2015. Besides, considering that the NMPBE occurs at the topside ionosphere, the plasma scale height might be lowered which also leads to larger plasma fluctuation of MSTID.

We further test the reliability of MSTID on the presence of the NMPBE. As introduced in section 1, only *Ne* profiles within 33°–47° magnetic latitude in the winter hemisphere are adopted for finding events. Thus,

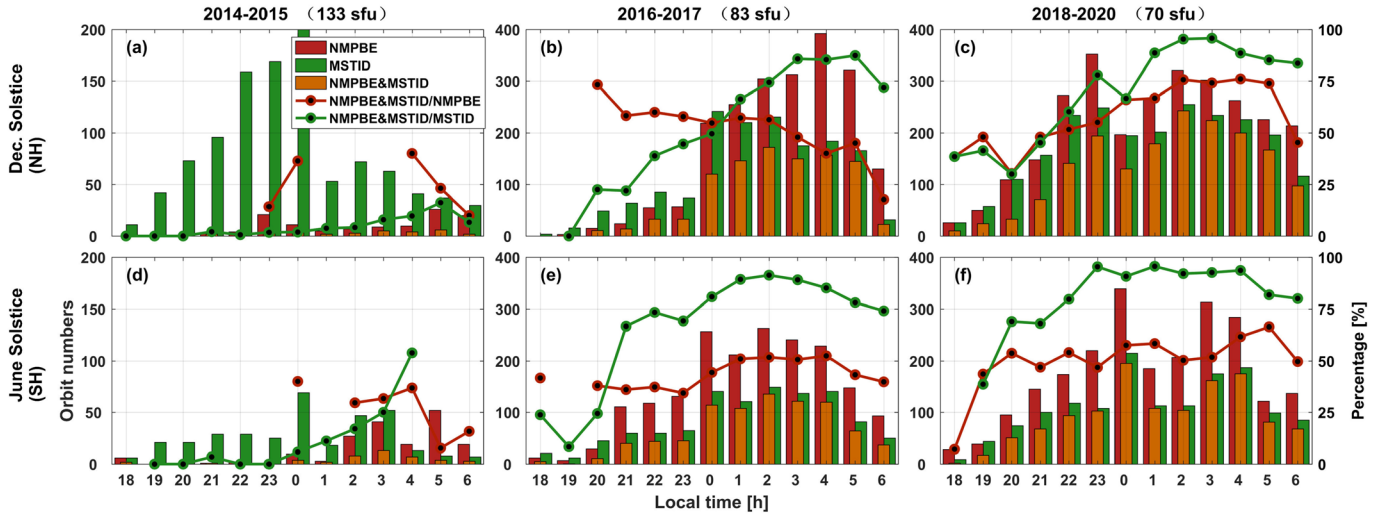

Figure 7. (a–f) Number of orbits when NMPBE (red bar), MSTID (green bar), or both (orange bar) are detected. Lines are the occurrence percentage of MSTID under the presence of NMPBE (red lines) and the occurrence percentage of NMPBE under the presence of MSTID (green lines). The occurrence percentage has not been calculated if the event number is less than 10.

only the MSTIDs that occur in 33–47° magnetic latitude in the winter hemisphere are considered. Figure 7 shows the number of orbits when the NMPBE with/or MSTID is detected in the winter hemisphere and their occurrence rate in percentages. The lines represent the percentage of orbit number when NMPBE and MSTID are simultaneously detected, with regard to the total number of NMPBE (red line) or MSTID (green line). Note that when the event number was lower than 10, the occurrence percentage is not calculated.

The plot shows that the number of NMPBE events prevails from midnight to postmidnight and experiences a tremendous increase from 2014–2015 to 2016–2017/2018–2020. This is consistent with Figures 3 and 5 that the longitudinal plasma enhancement starts to emerge from 2016–2017 at midnight and the results from Zhong et al. (2019). Meanwhile, MSTID shifted its local time preference from premidnight to postmidnight as time moves from 2014–2015 to 2016–2017 and 2018–2019. In other words, both the NMPBE and the MSTID in the winter hemisphere show postmidnight preference as solar activity decreases. The interesting thing is that for two solstices during 2016–2017 and 2018–2020, the occurrence of NMPBE among the MSTID events (green lines) is generally higher than the occurrence of MSTID among NMPBE events (red lines), which means that the majority of the MSTIDs are accompanied with NMPBE. From a perspective of local time variation, the green lines also show an enhancement from premidnight to postmidnight with a maximum value above 95%, which indicates that the MSTID is less affected by the NMPBE at earlier local time. In total, the above information also indicates that the NMPBE sets up a favorable condition for the MSTID at postmidnight, which made them more easily observed. Those MSTID should be generally embedded in the NMPBE as shown in Figure 1d since we set the same latitudinal window for the statistic.

The scenario might also answer the poor simultaneous coexisting of MEF/MFF with MSTID as reported previously. That is, although the occurrence of MEF/MMF shares similar climatology with that of MSTID, the MEF and MMF are not always accompanied by plasma fluctuations (Park et al., 2009; Saito et al., 1995). At the topside of the ionosphere, the plasma density and its vertical gradient are small so that the plasma density fluctuation of MSTID is small. Note that the space-borne observation of the plasma fluctuation is inspected manually in Saito et al. (1995) and automatically with absolute criteria in Park et al. (2009). Thus, the intensity of MEF/MMF might not be strong enough for causing observable plasma fluctuations when the ambient plasma density or its vertical gradient is low. The robust relative criteria for the detection should be adopted to test the detailed relationship between MSTID with MEF/MMF in the future.

Nevertheless, the scenario that enhanced the occurrence rate of MSTID is attributed to the higher background plasma density is not adequate enough. From a perspective of the local time variation, we note that in North America during December solstice of 2017–2020, the occurrence rate of MSTID is increased by 20% from midnight (Figure 2h) to predawn (Figure 2i), while the *Ne* (Figures 2h and 2r) stays the same. Besides,

the occurrence of MSTID in conjugating SH is lower at predawn (Figure 2i) than that at midnight (Figure 2h). Thus, neither the hemispheric coupling can explain that the frequent MSTID occurs at predawn in North America. Other mechanisms besides neither the *E-F* coupling nor the neutral wind contributed Perkins instability should be involved, which needs further exploration.

5. Conclusions

By applying an absolute criterion for the detection of MSTID, the current work presents comprehensive maps on the occurrence rate of MSTID during two solstices. Two interesting spatial structures of the MSTID's occurrence are highlighted: (1) regional preference near WSA to its west during December solstice, MSTID is this region even appears at very low latitudes and (2) band-like distribution and its symmetry/asymmetry depending on the solar cycle and local time. In detail, the first issue is a persistent phenomenon from 2014 to 2020. The latter issue shows variations on the solar flux. During 2014–2015, the occurrence of MSTID in the winter hemisphere is significantly lower than that in the summer hemisphere. However, as solar flux decreases and local time moves to the predawn sector, the occurrence of MSTID in the winter hemisphere shows stronger intensification compared to that in the summer hemisphere. Thus, the hemispheric asymmetry of the band-like distribution is reversed.

The calculation of the maximum neutral wind contributed Perkins instability from the model simulation shows a higher growth rate in the summer hemisphere with seasonal/longitudinal dependence. Taking into consideration *Es* via ionospheric *E-F* region coupling, we suggest that the first structure is associated with both the horizontal neutral wind and the *E-F* region coupling from the *Es* layer contributed Perkins instability. However, the simulation suggests that in the summer hemisphere, the neutral wind contribution to the Perkins instability is stronger at the predawn sector when the westward neutral wind dominates. The westward neutral wind is suitable for the growth of MSTID with the wavefront aligned in NE-SW (NW-SE) in the NH (SH), which is in a perpendicular direction to that of the previous observations (e.g., Shiokawa, Ihara, et al., 2003). There may exist some underlying issues that further works are needed to clarify this discrepancy out.

Since the growth of the neutral wind contribution to the Perkins instability is low in the winter hemisphere, then so as the *Es* activity. The key mechanism for causing the second structure involves the hemispheric coupling as well as the background plasma density. An abnormal feature is that the midlatitude Ne is higher during lower solar activity years when the NMPBE appears. The embedded MSTID should have a larger plasma density fluctuation amplitude; thus, a higher occurrence rate in the winter hemisphere is promised since we adopt the absolute criteria to detect MSTID. We suggest that the hemispheric coupling serves as the fundamental mechanism to generate plasma perturbations while the NMPBE makes it easier to be observed. However, at predawn during 2018–2020, the winter hemisphere shows the considerable higher occurrence of MSTID than that in the summer hemisphere, which neither the Perkins instability nor the presence of NMPBE is capable to explain.

Acknowledgments

The authors want to thank Dr. Jaeheung Park for constructive advice. The ESA is acknowledged for providing the Swarm data. The work of X. Wan and H. Wang is supported by the National Natural Science Foundation of China (41674153, 41521063, and 41431073). We thank the Technical University of Denmark for providing the source code of CHAOS-6 model on the website http://www.spacecenter.dk/files/magnetic-models/CHAOS-6/. F10.7 index is provided by NASA's OMNIweb (https://omniweb.gsfc.nasa.gov/ow_min.html). We also thank the World Data Center for Geomagnetism at Kyoto (http://wdc.kugi.kyoto-u.ac.jp/kp/index.html#LIST) for providing the *Kp* index.

Data Availability Statement

The data used in this study are the Swarm Level 1b electron density data, which are freely accessible online at (https://earth.esa.int/web/guest/swarm/data-access). The horizontal neutral wind data simulated by the TIEGCM are uploaded to https://data.4tu.nl/ with the following DOI (10.4121/uuid:e52de14b-5f74-42df-9c58-c2fad90cfae4).

References

Arras, C., Wickert, J., Beyerle, G., Heise, S., Schmidt, T., & Jacobi, C. (2008). A global climatology of ionospheric irregularities derived from GPS radio occultation. *Geophysical Research Letters*, *35*, L14809. https://doi.org/10.1029/2008GL034158

Burke, W. J., Martinis, C. R., Lai, P. C., Gentile, L. C., Sullivan, C., & Pfaff, R. F. (2016). C/NOFS observations of electromagnetic coupling between magnetically conjugate MSTID structures. *Journal of Geophysical Research: Space Physics*, *121*, 2569–2582. https://doi.org/10.1002/2015JA021965

Chen, C. H., Huba, J. D., Saito, A., Lin, C. H., & Liu, J. Y. (2011). Theoretical study of the ionospheric Weddell Sea Anomaly using SAMI2. *Journal of Geophysical Research*, *116*, A04305. https://doi.org/10.1029/2010ja015573

Cosgrove, R. B. (2007). Generation of mesoscale *F* layer structure and electric fields by the combined Perkins and *Es* layer instabilities, in simulations. *Annales de Geophysique*, *25*(7), 1579–1601. https://doi.org/10.5194/angeo-25-1579-2007

Cosgrove, R. B., & Tsunoda, R. T. (2004). Instability of the *E-F* coupled nighttime midlatitude ionosphere. *Journal of Geophysical Research*, *109*, A04305. https://doi.org/10.1029/2003JA010243

Fuller-Rowell, T. J. (1998). The "thermospheric spoon": A mechanism for the semiannual density variation. *Journal of Geophysical Research*, *103*(A3), 3951–3956. https://doi.org/10.1029/97JA03335

Garcia, F. J., Kelley, M. C., Makela, J. J., & Huang, C.-S. (2000). Airglow observations of mesoscale low-velocity traveling ionospheric disturbances at midlatitudes. *Journal of Geophysical Research*, *105*(A8), 18,407–18,415. https://doi.org/10.1029/1999JA000305

Haldoupis, C., & Schlegel, K. (1996). Characteristics of midlatitude coherent backscatter from the ionospheric *E* region obtained with sporadic *E* scatter experiment. *Journal of Geophysical Research*, *101*(A6), 13,387–13,397. https://doi.org/10.1029/96JA00758

Heelis, R. A., Lowell, J. K., & Spiro, R. W. (1982). A model of the high-latitude ionospheric convection pattern. *Journal of Geophysical Research*, *87*(A8), 6339–6345. https://doi.org/10.1029/JA087iA08p06339

Hernández-Pajares, M., Juan, J. M., Sanz, J., & Aragón-Àngel, A. (2012). Propagation of medium scale traveling ionospheric disturbances at different latitudes and solar cycle conditions. *Radio Science*, *47*, RS0K05. https://doi.org/10.1029/2011RS004951

Jiang, G., Xu, J., Wang, W., Yuan, W., Zhang, S., Yu, T., et al. (2018). A comparison of quiet time thermospheric winds between FPI observations and model calculations. *Journal of Geophysical Research: Space Physics*, *123*, 7789–7805. https://doi.org/10.1029/2018JA025424

Kelley, M. C., Haldoupis, C., Nicolls, M. J., Makela, J. J., Belehaki, A., Shalimov, S., & Wong, V. K. (2003). Case studies of coupling between the *E* and *F* regions during unstable sporadic-*E* conditions. *Journal of Geophysical Research*, *108*(A12), 1447. https://doi.org/10.1029/2003JA009955

Kelley, M. C., & Makela, J. J. (2001). Resolution of the discrepancy between experiment and theory of midlatitude *F* region structures. *Geophysical Research Letters*, *28*(13), 2589–2592. https://doi.org/10.1029/2000GL012777

Kil, H., & Paxton, L. J. (2017). Global distribution of nighttime medium-scale traveling ionospheric disturbances seen by Swarm satellites. *Geophysical Research Letters*, *44*, 9176–9182. https://doi.org/10.1002/2017GL074750

Kotake, N., Otsuka, Y., Tsugawa, T., Ogawa, T., & Saito, A. (2006). Climatological study of GPS total electron content variations caused by medium-scale traveling ionospheric disturbances. *Journal of Geophysical Research*, *111*, A04306. https://doi.org/10.1029/2005JA011418

Kotake, N., Otsuka, Y., Tsugawa, T., Ogawa, T., & Saito, A. (2007). Statistical study of medium-scale traveling ionospheric disturbances observed with the GPS networks in Southern California. *Earth, Planets and Space*, *59*(2), 95–102. https://doi.org/10.1186/BF03352681

Makela, J. J., & Otsuka, Y. (2012). Overview of nighttime ionospheric instabilities at low- and mid-latitudes: Coupling aspects resulting in structuring at the mesoscale. *Space Science Reviews*, *168*(1–4), 419–440. https://doi.org/10.1007/s11214-011-9816-6

Martinis, C., Baumgardner, J., Wroten, J., & Mendillo, M. (2010). Seasonal dependence of MSTIDs obtained from 630.0 nm airglow imaging at Arecibo. *Geophysical Research Letters*, *37*, L11103. https://doi.org/10.1029/2010GL043569

Niu, J., Weng, L. B., Meng, X., & Fang, H. X. (2019). Morphology of ionospheric sporadic *E* layer intensity based on COSMIC occultation data in the middle-and low-latitude regions. *Journal of Geophysical Research: Space Physics*, *124*, 4796–4808. https://doi.org/10.1029/2019JA026828

Otsuka, Y., Shiokawa, K., Ogawa, T., & Wilkinson, P. (2004). Geomagnetic conjugate observations of medium-scale traveling ionospheric disturbances at midlatitude using all-sky airglow imagers. *Geophysical Research Letters*, *31*, L15803. https://doi.org/10.1029/2004GL020262

Park, J., Lühr, H., Kervalishvili, G., Rauberg, J., Michaelis, I., Stolle, C., & Kwak, Y.-S. (2015). Nighttime magnetic field fluctuations in the topside ionosphere at midlatitudes and their relation to medium-scale traveling ionospheric disturbances: The spatial structure and scale sizes. *Journal of Geophysical Research: Space Physics*, *120*, 6818–6830. https://doi.org/10.1002/2015JA021315

Park, J., Lühr, H., Min, K. W., & Lee, J.-J. (2010). Plasma density undulations in the nighttime mid-latitude *F*-region as observed by CHAMP, KOMPSAT-1, and DMSP F15. *Journal of Atmospheric and Terrestrial Physics*, *72*(2–3), 183–192. https://doi.org/10.1016/j.jastp.2009.11.007

Park, J., Lühr, H., Stolle, C., Rother, M., Min, K. W., Chung, J.-K., et al. (2009). Magnetic signatures of medium-scale traveling ionospheric disturbances as observed by CHAMP. *Journal of Geophysical Research*, *114*, A03307. https://doi.org/10.1029/2008JA013792

Perkins, F. (1973). Spread *F* and ionospheric currents. *Journal of Geophysical Research*, *78*(1), 218–226. https://doi.org/10.1029/JA078i001p00218

Richards, P. G., Fennelly, J. A., & Torr, D. G. (1994). EUVAC: A solar EUV flux model for aeronomic calculations. *Journal of Geophysical Research*, *99*(A5), 8981–8992. https://doi.org/10.1029/94JA00518

Saito, A., Iyemori, T., Blomberg, L. G., Yamamoto, M., & Takeda, M. (1998). Conjugate observations of the mid-latitude electric field fluctuations with the MU radar and the Freja satellite. *Journal of Atmospheric and Solar - Terrestrial Physics*, *60*(1), 129–140. https://doi.org/10.1016/S1364-6826(97)00094-1

Saito, A., Iyemori, T., Sugiura, M., Maynard, N. C., Aggson, T. L., Brace, L. H., et al. (1995). Conjugate occurrence of the electric field fluctuations in the nighttime midlatitude ionosphere. *Journal of Geophysical Research*, *100*(A11), 21,439–21,451. https://doi.org/10.1029/95JA01505

Shiokawa, K., Ihara, C., Otsuka, Y., & Ogawa, T. (2003). Statistical study of nighttime medium-scale traveling ionospheric disturbances using midlatitude airglow imagers. *Journal of Geophysical Research*, *108*(A1), 1052. https://doi.org/10.1029/2002JA009491

Shiokawa, K., Otsuka, Y., Ihara, C., Ogawa, T., & Rich, F. J. (2003). Ground and satellite observations of nighttime medium-scale traveling ionospheric disturbance at midlatitude. *Journal of Geophysical Research*, *108*(A4), 1145. https://doi.org/10.1029/2002JA009639

Shiokawa, K., Otsuka, Y., Tsugawa, T., Ogawa, T., Saito, A., Ohshima, K., et al. (2005). Geomagnetic conjugate observation of nighttime medium-scale and large-scale traveling ionospheric disturbances: FRONT3 campaign. *Journal of Geophysical Research*, *110*, A05303. https://doi.org/10.1029/2004JA010845

Stolle, C., Lühr, H., Rother, M., & Balasis, G. (2006). Magnetic signatures of equatorial spread *F* as observed by the CHAMP satellite. *Journal of Geophysical Research*, *111*, A02304. https://doi.org/10.1029/2005JA011184

Su, S.-Y., Liu, C. H., Ho, H. H., & Chao, C. K. (2006). Distribution characteristics of topside ionospheric density irregularities: Equatorial versus midlatitude regions. *Journal of Geophysical Research*, *111*, A06305. https://doi.org/10.1029/2005JA011330

Tsai, L.-C., Su, S.-Y., Liu, C.-H., Schuh, H., Wickert, J., & Alizadeh, M. M. (2018). Global morphology of ionospheric sporadic *E* layer from the FormoSat-3/COSMIC GPS radio occultation experiment. *GPS Solutions*, *22*(4), 118. https://doi.org/10.1007/s10291-018-0782-2

Tsunoda, R. T., & Cosgrove, R. B. (2001). Coupled electrodynamics in the nighttime midlatitude ionosphere. *Geophysical Research Letters*, *28*(22), 4171–4174. https://doi.org/10.1029/2001GL013245

Wan, X., Xiong, C., Rodriguez-Zuluaga, J., Kervalishvili, G. N., Stolle, C., & Wang, H. (2018). Climatology of the occurrence rate and amplitudes of local time distinguished equatorial plasma depletions observed by Swarm satellite. *Journal of Geophysical Research: Space Physics*, *123*, 3014–3026. https://doi.org/10.1002/2017JA025072

Watson, C., & Pedatella, N. M. (2018). Climatology and characteristics of medium-scale *F* region ionospheric plasma irregularities observed by COSMIC radio occultation receivers. *Journal of Geophysical Research: Space Physics*, *123*, 8610–8630. https://doi.org/10.1029/2018JA025696

Wu, D. L., Ao, C. O., Hajj, G. A., de la Torre Juarez, M., & Mannucci, A. J. (2005). Sporadic *E* morphology from GPS-CHAMP radio occultation. *Journal of Geophysical Research*, *110*, A01306. https://doi.org/10.1029/2004JA010701

Xiong, C., Luhr, H., & Fejer, B. G. (2015). Global features of the disturbance winds during storm time deduced from CHAMP observations. *Journal of Geophysical Research: Space Physics*, *120*, 5137–5150. https://doi.org/10.1002/2015JA021302

Xiong, C., Lühr, H., Sun, L., Luo, W., Park, J., & Hong, Y. (2019). Long-lasting latitudinal four-peak structure in the nighttime ionosphere observed by the Swarm constellation. *Journal of Geophysical Research: Space Physics*, *124*, 9335–9347. https://doi.org/10.1029/2019JA027096

Yokoyama, T., Hysell, D. L., Otsuka, Y., & Yamamoto, M. (2009). Three-dimensional simulation of the coupled Perkins and *Es*-layer instabilities in the nighttime midlatitude ionosphere. *Journal of Geophysical Research*, *114*, A03308. https://doi.org/10.1029/2008JA013789

Yokoyama, T., & Stolle, C. (2017). Low and midlatitude ionospheric plasma density irregularities and their effects on geomagnetic field. *Space Science Reviews*, *206*(1–4), 495–519. https://doi.org/10.1007/s11214-016-0295-7

Zhong, J., Lei, J., Yue, X., Luan, X., & Dou, X. (2019). Middle-latitudinal enhancement observed in the nighttime ionosphere. *Journal of Geophysical Research: Space Physics*, *124*, 5857–5873. https://doi.org/10.1029/2018JA026059

Zhou, C., Tang, Q., Song, X., Qing, H., Liu, Y., Wang, X., et al. (2016). A statistical analysis of sporadic *E* layer occurrence in the midlatitude China region. *Journal of Geophysical Research: Space Physics*, *122*, 3617–3631. https://doi.org/10.1002/2016JA023135